Crack initiation, propagation, and arrest in sintering powder aggregates

Joseph R Carazzone, Christophe L. Martin, Zachary C Cordero

Received: 30 December 2019 | Revised: 8 April 2020 | Accepted: 9 April 2020

DOI: 10.1111/jace.17170

ORIGINAL ARTICLE

Journal of the American Ceramic Society

Crack initiation, propagation, and arrest in sintering powder aggregates

Joseph R. Carazzone[1] | Christophe L. Martin[2] | Zachary C. Cordero[1]

[1]Department of Materials Science and NanoEngineering, Rice University, Houston, TX, USA

[2]Université Grenoble Alpes, CNRS, Grenoble INP, SIMaP, Grenoble, France

Correspondence
Zachary C. Cordero, Department of Materials Science and NanoEngineering, Rice University, 6100 Main Street, MS 325, 77005, Houston, TX, USA.
Email: zc29@rice.edu

Funding information
Division of Civil, Mechanical and Manufacturing Innovation, Grant/Award Number: 1826064; Rice University

Abstract

Cracking during sintering is a common problem in powder processing and is usually caused by constraint that prevents the sintering material from shrinking in one or more directions. Different factors influencing sintering-induced cracking include temperature schedule, packing density, and specimen geometry. Here we use the discrete element method to directly observe the stress distribution and sinter-cracking behavior in edge notched panels sintered under a uniaxial restraint. This geometry allows an easy comparison with traditional fracture mechanics parameters, facilitating analysis of sinter-cracking behavior. We find that cracking caused by self-stress during sintering resembles the growth of creep-cracks in fully dense materials. By deriving the constrained densification rate from the appropriate constitutive equations, we discover that linear shrinkage transverse to the loading axis is accelerated by a contribution from the effective Poisson's ratio of a sintering solid. Simulation of different notch geometries and initial relative densities reveals conditions that favor densification and minimize crack growth, alluding to design methods for avoiding cracking in actual sintering processes. We combine the far-field stress and crack length to compute the net section stress, finding that it characterizes the stress profile between the notches and correlates with the sinter-crack growth rate, demonstrating its potential to quantitatively describe sinter-cracking.

KEYWORDS

discrete element method, fracture, glass, powder processing, sintering

1 | INTRODUCTION

Solid-state sintering is commonly used to densify and strengthen weakly bound, near-net shaped powder aggregates. The driving force for sintering is surface energy minimization: a powder aggregate possesses excess surface area which can be eliminated by mass transport mechanisms active at elevated temperatures, leading to the growth of contacts between powder particles and the overall shrinkage of the sintering article.[1-4] In practice, a sintering material can experience various forms of restraint which inhibit its shrinkage (a phenomenon referred to as "constrained sintering"), leading to the generation of internal stress.[5,6] Sources of restraint include friction between the sintering material and its substrate,[5] non-densifying inclusions,[7] and differential sintering rates between different material components.[8] Under certain conditions, this self-induced stress becomes large enough to cause the initiation and growth of cracks.[7,9] This process, termed sinter-cracking, is typically observed during the early stages of sintering, when the bonds between particles are weakest.[10-12]

The process of sinter-cracking comprises two stages—initiation and growth. Sinter-cracks typically initiate near stress concentrators present either at the microscale (eg, as powder

JACE | Journal Name | Manuscript No. 17170 | WILEY | Dispatch: 26-4-2020 | No. of pages: 20 | CE: Vanitha Shree | PE: Raghu B.

agglomerates,[10,13] rigid inclusions,[7,14] and spatial variations in packing density or particle size[15,16]) or at the macroscale (eg, as design features like notches[9,10,17]). Sinter-crack initiation is influenced by the pore size distribution and the initial relative density of the powder aggregate. For example, Wang and Atkinson discovered that for constrained sintering, pores tend to grow rather than shrink when their initial size exceeds a critical value.[18] Sudre et al considered the porous matrix of a sintering composite and found that high initial relative densities mitigate sinter-crack initiation by decreasing the extent of differential densification.[6]

After a sinter-crack has initiated, it can then grow through a process that closely resembles creep-cracking in fully dense materials. Bordia and Jagota, for instance, observed sinter-crack growth in alumina films and found that sinter-cracks grew by the coalescence of pores in a process zone ahead of the main crack, similar to the linking up of grain boundary cavities ahead of a creep-crack.[9,19] More quantitative, fracture mechanics–based analyses of sinter-cracking further support this similarity between sinter-cracking and creep-cracking. Ostertag et al used the stress intensity factors for a plane strain radial crack emanating from a central heterogeneity to compute the stress intensity required for sinter-crack growth in MgO and found that this stress intensity was similar to that required for creep-crack growth.[7] Similarly, Jagota and Hui used fracture mechanics to analyze sinter-crack growth in a glass powder film containing a central crack and demonstrated that the stress intensity produced by sintering ahead of the crack is not large enough to cause brittle fracture, favoring instead crack growth by a creeping damage mechanism.[20]

Recently, the initiation and propagation of sinter-cracks were observed directly via in situ monitoring of a powder aggregate sintering under restraint.[21] The experiment revealed how sinter-cracks initiate following an incubation period of densification, then propagate through a ductile fracture mode, characterized by high material elongation and interrupted by phases of crack arrest and shrinkage. From this macroscopic view of sinter-cracking in progress, new questions arise. How does the microstructure evolve around the crack and in the sintering material? What is the stress experienced by the material and how is it distributed? How does the stress evolve and can it be related to the crack growth rate? Addressing these questions requires knowledge of particle-scale phenomena difficult to access experimentally, making computational simulations a valuable complement.

Several investigators have analyzed continuum aspects of sinter-crack initiation and growth using the finite element[6,12,20] and material point[15] methods; however, these methods are inherently limited in their treatment of sinter-cracking because they rely on macroscopic approximations of shrinkage behavior and cannot directly capture activity at the particle level, such as the evolution of particle contacts, on which sinter-cracking depends. By contrast, the discrete element method (DEM) is well-suited for studying a sintering powder aggregate, especially at the early stages of sintering when the material is particulate and particle rearrangement plays a significant role. As in real sintering, DEM allows the powder aggregate to evolve based on the forces acting on particle contacts, so that macroscopic behavior is the result of microscopic activity at the particle length scale, without continuum approximations. These contact forces are defined by constitutive laws derived from sintering theory, are calculated for the entire system of particles simultaneously at each step, and give rise to particle movement according to Newton's equations of motion.[22] DEM can accurately represent the random nature of a real powder aggregate and can probe the mechanical and structural properties of sintered aggregates.[23,24] It naturally incorporates phenomena such as particle rearrangement, contact breakup and formation, and interaction between neighboring contacts.[25]

Using DEM, Henrich et al found that for a constrained sintering specimen containing a stress-concentrator, cracking was inhibited by a low tangential viscosity at the contacts between particles, which allowed particle rearrangement and prevented the buildup of stress near the stress-concentrator.[22] In a similar study, Martin et al also found particle rearrangement to favor sintering without cracking, but observed crack initiation due to local packing heterogeneity and greater crack propagation caused by greater initial relative density of the specimen.[25] They found that a large void in the specimen will close during sintering when there is no constraint on densification and particle rearrangement is maximized, suggesting a regime for sinter-crack healing. Rasp et al used DEM to look at cracking in films containing cylindrical cavities sintering on rigid substrates.[26] In addition to the effect of particle rearrangement observed previously, they found that incorporating small cracks in the specimen microstructure was necessary to reproduce experimentally observed behavior.

The objective of this paper is to determine the cause and nature of sinter-crack initiation, propagation, and arrest by using DEM to investigate the structural evolution of a sintering powder aggregate under the influence of constraint and stress-concentration. We first consider the difference between free and constrained sintering by looking at densification that occurs with particle contact growth. Then, we test a range of stress-concentrator dimensions under constrained sintering conditions to determine the effect of stress concentration on densification, stress evolution, and cracking behavior. From this, we identify the appropriate stress parameter for describing the effect of the stress-concentrator on sinter-crack propagation. Using fracture mechanics, we examine the effect of the stress-concentrator on specimen compliance and how it relates to the stress evolution. We then briefly explore the dependence of the crack growth rate on the initial relative density of the specimen. Finally, we examine the microscopic stress field around the notches to determine the characteristic

stress parameter, and then demonstrate a correlation between this parameter and the crack growth rate, a correlation which points to the appropriate framework for describing and predicting sinter-crack behavior.

2 | COMPUTATIONAL METHODS

Structural evolution and sinter-crack behavior were investigated using the in-house DEM code dp3D developed at SIMAP laboratory. Particles are modeled as spheres interacting with each other through their contacts during sintering. At each time step, the sum of contact forces determines the acceleration of particles. The code uses an explicit scheme with dynamic resolution of velocities and positions for each particle. Further details concerning the methodology can be found in earlier works.[27,28]

The simulation specimens were thin double edge notched panels like the one shown in Figure 1. The edge notched panels were composed of spherical particles and were sintered under uniaxial restraint while damage evolution at the notches was assessed as a function of sintering time and specimen relative density. The net section stress in the midplane of the specimens was measured by exploiting the ability of DEM to compute the forces acting on individual particles. This quantity was compared with the sinter-crack growth rate to understand the fracture mechanism.

2.1 | Specimen preparation

Figure 1 gives the relevant dimensions of the edge notched specimens, with the height, thickness, and width represented by H, B, and $2W$, respectively. The height and length of each edge notch are represented by b and d. Each specimen began as a gas of 75 000 randomly placed 5 μm diameter particles having a relative density of 0.30. The gas was condensed by a slow isostatic compaction at a macroscopic pressure much less than the particle elastic modulus to ensure that densification is solely driven by particle rearrangement. Boundary conditions were fully periodic and compaction was carried out to a relative density of 0.62 by shrinking the periodic box. The panel specimens were further densified to relative densities of 0.65, 0.70, and 0.75 by an affine displacement of particles. This method of specimen preparation, which is the same as that used by Martin and Bordia in their study of films sintered on rigid substrates,[30] gives an isotropic, homogeneous, randomly packed particle aggregate. During the affine displacement and in the subsequent sintering step, the relative density was computed based on the material contained within a reference sphere centered in the middle of the specimen, far from the edge notches (cf. Figure 1). The reference sphere initially contained ~ 950 particles. Note that if a particle resided on the surface of the sphere, only its portion inside the reference sphere was considered in the density calculation. Material properties used for these specimen preparation steps are given in the Supplementary Material.

The specimens were approximately 85 particles tall, 55 particles wide, and 15 particles thick. The thicknesses of the specimens before sintering were between 60 and 70 μm, similar to the thickness of tape-cast barium cerate–based films used in hydrogen separation devices[31] and of screen-printed zirconia films used in solid oxide fuel cells,[32] materials systems in which sinter-cracking can be

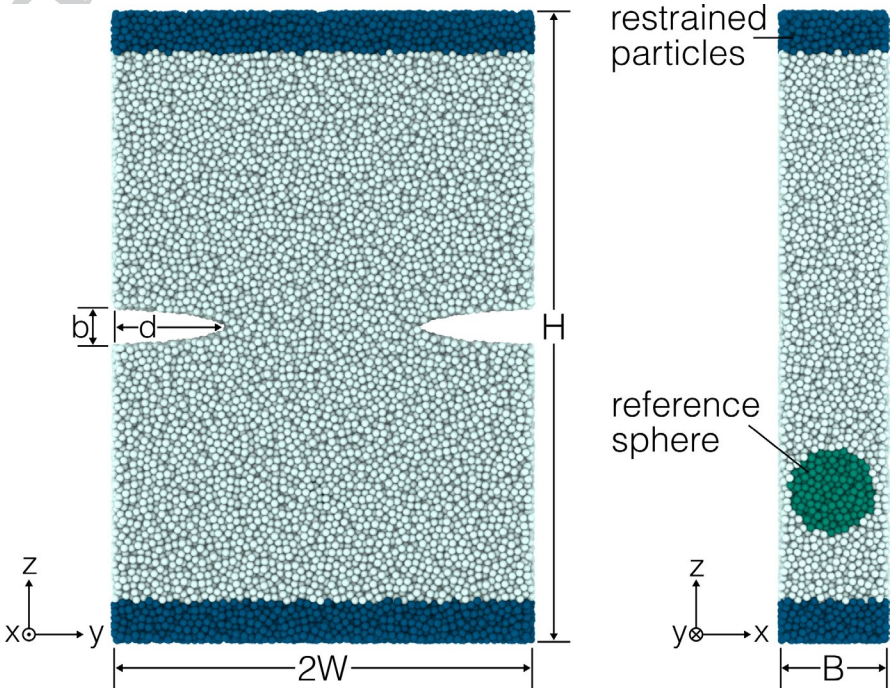

FIGURE 1 Double edge notched panel composed of spherical glass particles. Relevant dimensions are indicated: specimen height H, width $2W$, and thickness B, as well as notch height b and length d. Dark blue particles at the top and bottom were prevented from moving in the z-direction to produce a state of uniaxial restraint. The side view is a cross section through the middle of the panel. The dark green particles are contained within the reference sphere, used for measuring relative density. Renderings were produced using OVITO[29]

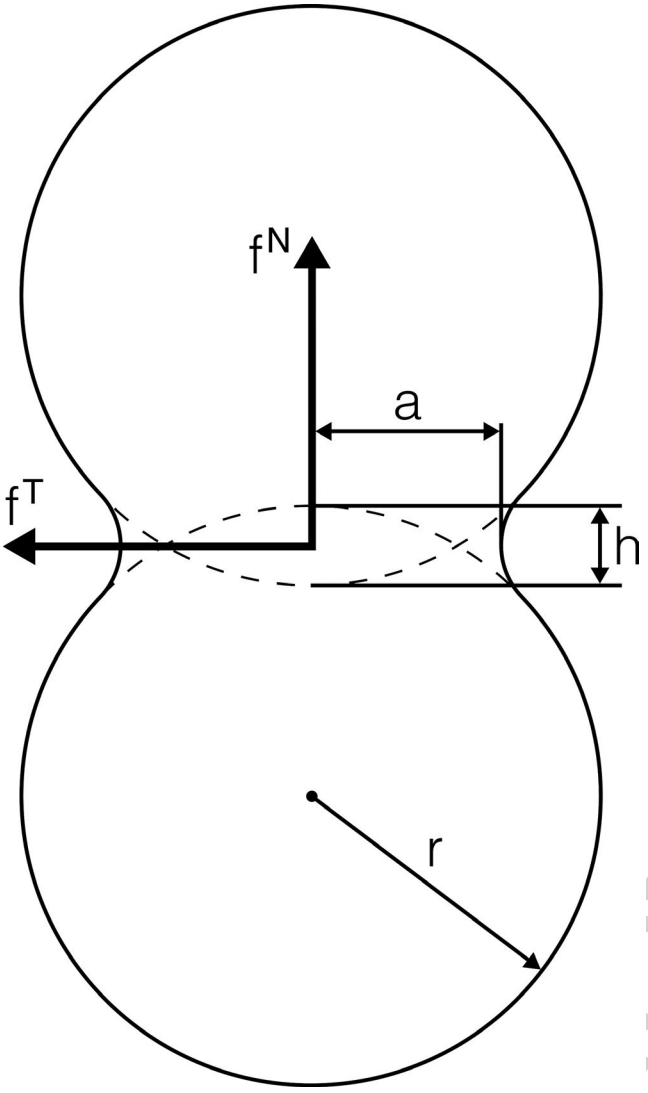

FIGURE 2 Particle contact geometry showing directions of the normal (*N*) and tangential (*T*) forces *f* acting at the contact. The diagram indicates particle radius *r*, contact radius *a*, and length of particle overlap *h*. Curvature of the neck represents the Coble contact geometry

a problem.[18,33] The specimen dimensions were chosen to minimize sample size effects. Specimen height was such that further increases in its value did not change the cracking behavior for the greatest notch height considered. The specimen thickness was large enough that further increase in thickness did not significantly influence the cracking behavior, although there was still a thickness effect in which crack length after a given amount of densification tended to increase with thickness, all other factors being constant. After the preparation steps described above, edge notches were introduced into the panel specimens by removing particles contained within extruded ellipses centered on the specimen edges. Notch geometries were generated with heights of 3, 5, and 10 particles and lengths ranging from 1 to 15 particles.

2.2 | Contact law

The contact law used in this work was developed by Jagota et al to describe the early stage of viscous sintering, in which the material can be approximated as an assemblage of particles.[2] In this regime, the sintering material is well characterized by the contact area between particles as a state variable, as opposed to the final stage of sintering, when the material is better characterized by its porosity. The law has been used previously to investigate viscosities and sintering rates in composite packings of viscous spheres.[34] Viscous sintering applies to glass materials and is well understood, making it a good model case.[35]

Figure 2 illustrates the geometry of a single particle contact and the forces acting on it. Following Jagota et al,[2] the equations for the normal and tangential forces, f^N and f^T, are given as.

$$f^N = \frac{3\pi}{2}\frac{dh}{dt}a\eta - \frac{3\pi}{2}0.83a\gamma, \quad (1)$$

$$f^T = -\frac{\pi}{2}\frac{du}{dt}a\eta, \quad (2)$$

where η is the shear viscosity of the fully dense material, γ is the surface energy, and a is the contact radius. $\frac{dh}{dt}$ is the normal component of the relative velocity between particles and corresponds to particle coalescence; $\frac{du}{dt}$ is the tangential component of the relative velocity and contributes to particle rearrangement. The contact radius a is related to the length of particle overlap h through Coble's geometric model of neck growth:[36]

$$\frac{da}{dt} = \frac{r}{a}\frac{dh}{dt}, \quad (3)$$

for particle radius r and time t. The extrinsic strain rate term included in the original contact law developed by Jagota et al have been omitted from Equations 1 and 2. The extrinsic strain rate represents the part of the total strain rate at one contact that is due to the strain occurring at other contacts on the same particles.[2] Omission of the extrinsic strain rate is justified because DEM naturally accounts for these interactions.

The viscous sintering contact law presented in Equations 1 and 2 is valid while the material remains particulate and deformation occurs mainly at the particle contacts. Viscous flow, the mechanism by which viscous sintering occurs, can occur almost anywhere within a glass particle at sintering temperatures.[1] However, finite element analysis of the viscous sintering of two spherical particles has shown that, for a normalized contact radius ranging from 0.01 to 0.5, the deformation of the particles due to sintering is localized in a small region near the neck.[37] For all results reported here, the average normalized geometric contact radius of the specimen

lies within this range. Finally, we note that the sintering term in Equation 1 (containing γ) implies that the sintering force increases with the contact radius *a*. This effect has been confirmed computationally for viscous sintering in the range of normalized contact radius considered here.[1]

2.3 | Simulation conditions

Equations 1 and 2 were evaluated using material properties for soda lime glass given by McLellan and Shand, summarized in Table 1.[38] The shear viscosity η of the fully dense glass was calculated using the Arrhenius model:

$$\eta = \eta_0 \exp\left(\frac{Q}{RT}\right), \tag{4}$$

where η_0 is the pre-exponential constant, Q is the activation energy, R is the gas constant, and T is the absolute temperature. Specimens were sintered under free and constrained loading conditions at a temperature of 700°C, near the softening point of the selected glass, where Equation 4 gives the value of η as 6.90 MPa s.

Following other DEM investigations, sintering was carried out to a relative density of 0.90, which is suitable for models describing a material having open porosity.[22,26] The present contact law has been shown to agree well with experiments and with other theoretical models of viscous sintering for the linear shrinkages and range of relative density considered in this work.[2,37,39] Theoretical work has shown that for spherical particles, neighboring contacts begin to impinge on one another at a relative density of 0.90, indicating that the assumption of discrete contacts is valid until this point.[40] This relative density corresponds to an average normalized contact radius of 0.5 for spherical particles, which is the applicability limit determined by finite element analysis for the present contact law.[37,41] Recent observations with X-ray microtomography found that separated contacts on sintering glass spheres begin to coalesce at a relative density of 0.75; however, mostly open porosity was observed until a relative density of 0.90, consistent with our application of DEM to this range.[42]

TABLE 1 Material properties for soda lime glass, obtained from McLellan and Shand[38]

Material property	Symbol	Value
Theoretical density (g/cm^3)	ρ_t	2.5
Surface energy (J/m^2)	γ	0.3
Pre-exponential, viscosity (MPa s)	η_0	1.05×10^{-14}
Activation energy, viscosity (kJ/mol)	Q	276
Viscosity[a] (MPa s)	η	6.90

[a]According to the Arrhenius model.

Fixed grip loading conditions were achieved by selecting layers of particles at the top and bottom of the specimen and imposing on them a condition of zero-displacement in the *z*-direction. Each layer was five particles thick and is shown in dark blue in Figure 1. This loading configuration results in a state of uniaxial tensile stress far from the notches, thereby simplifying analysis of stress evolution and cracking behavior. The simulations were conducted after removing the periodic boundary conditions initially used to generate the numerical specimen. We note that while the model of Jagota et al was developed for the case of an isotropic sintering material, it is nonetheless applicable to the present case of anisotropic boundary conditions: anisotropy is allowed to evolve in the system because of the discrete elements themselves, to which the isotropic model is applied.

2.4 | Stress measurements

The stress in the specimen was determined by means of the local particle stress tensor $\boldsymbol{\sigma}$, calculated for each particle i as follows:[43]

$$\boldsymbol{\sigma}_i = \frac{1}{V^*} \times \sum_{j \neq i} \boldsymbol{f}_{ij} \boldsymbol{x}_{ij}, \tag{5}$$

where $\boldsymbol{f}$ is the force vector acting on the contact between particles i and j, and $\boldsymbol{x}$ is the position vector connecting their centers. The force vector $\boldsymbol{f}$ derives directly from Equations 1 and 2. The summation acts on the vector product $\boldsymbol{f}_{ij}\boldsymbol{x}_{ij}$ for all particles j in contact with particle i. The representative volume V^* is the Voronoi cell volume computed for particle i using tessellations obtained with the Voro++ package.[44] Thus, Equation 5 accounts for the local variations in packing density that evolve during sintering. Dimensional analysis of Equation 5 reveals that the second term in Equtaion 1 gives a $1/r$ dependence to $\boldsymbol{\sigma}$. Thus, the magnitude of the stress is expected to increase as the particle size decreases for a monodisperse aggregate, but the distribution of the stress within the aggregate is expected to remain the same.

A continuum representation of the *zz* stress component in the specimen was obtained by averaging $\boldsymbol{\sigma}$ over discrete volumes. The averaging volume was a 10-μm cube (twice the particle diameter). The cube was centered in the *x* dimension of the specimen and moved through the *y* and *z* dimensions by steps of 5 μm, omitting particles within 5 μm of the specimen surfaces to avoid free-surface effects. At each step, the arithmetic mean was calculated for the *zz* component of $\boldsymbol{\sigma}$ for all particles with centers lying inside the cube, yielding σ_{ave}. By considering only those particles for which $|x| < 5$ μm, the effects of the free *x*-normal

surfaces of the specimen were omitted. The far-field stress σ_{far} was calculated by averaging σ_{ave} over the regions between the notches and the fixed particle layers, for which 100 μm < |z| < 150 μm. This was to avoid stress concentration effects from the notches and surface effects from the fixed particle layers. The stress profile $\overline{\sigma}$ in the notch region, for which |z| < 30 μm, was determined as the maximum σ_{ave} at each position y in the notch region.

2.5 | Sinter-crack length

The length of the sinter-crack was determined by monitoring the geometric separation of particles (ie, the failure criterion for a sintered contact is simply given by the condition that the interparticle distance is greater than the sum of their radii). The notch roots were regarded as the points of crack initiation because particle separation events were concentrated in this area. While such separation events occurred elsewhere in the specimen, their frequency was low enough to disregard them. The initiation of the sinter-crack was determined by monitoring for particle separation within one particle diameter of the original notch root. Subsequent particle separation events were regarded as part of the main crack if they occurred within one particle diameter of previous separation events. The length of the sinter-crack was taken as the horizontal distance between the instantaneous positions of the crack tip and the notch root.

3 | RESULTS AND DISCUSSION

3.1 | Densification behavior

3.1.1 | Free sintering

We first consider the densification behavior of specimens without edge notches sintering under free and constrained conditions. The relative density ρ as measured by the reference sphere is plotted in Figure 3 against a dimensionless time τ, defined as

$$\tau = \frac{\gamma}{\eta r}\left(\frac{3}{4\pi}\right)^{1/3} t, \tag{6}$$

where t is the time in seconds.[2] The free sintering curve starting at initial relative density $\rho_0 = 0.62$ shows a positive curvature similar to that for specimens with ρ_0 equal to 0.65, 0.70, and 0.75. The continuum average calculation of Jagota et al for the case of free sintering is shown for comparison with the simulation.[2]

The free densification curves given by Jagota et al and the present DEM are consistent in their form, both displaying

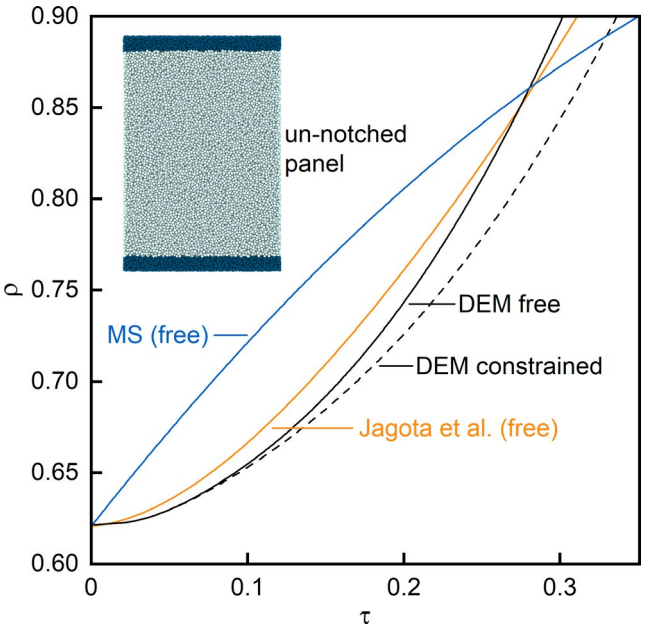

COLOR online, B&W in print

FIGURE 3 Relative density ρ vs reduced time τ for the unnotched panel (inset) during free and constrained sintering. Data from the discrete element simulation are labeled as DEM. Shown for comparison are the continuum average calculation of Jagota et al for the same contact law[2] and the spherical pore model of Mackenzie and Shuttleworth[45] (MS), both for the case of free sintering. The initial relative density in each case is 0.62

positive curvature and both reaching $\rho = 0.90$ around $\tau = 0.3$. However, the DEM curve begins with a slower densification rate which accelerates gradually, surpassing that of the continuum curve at $\tau = 0.18$. This reveals an important distinction between the continuum average calculation and the DEM simulation due to the consideration of particle rearrangement. The continuum average calculation of Jagota et al considers a constant particle coordination number of 7.3 and a starting relative density of 0.62 (although the coordination number for such relative densities is often lower[46]). Conversely, the DEM simulation tracks a change in average coordination number from 5.7 to 7.9 over the course of sintering. The average coordination number at the beginning of the simulation is less than the value assumed by Jagota et al, causing the total driving force for densification (hence the densification rate) to be less than that determined by their calculation. As the average coordination number increases, the total driving force for sintering increases, causing the densification rate to accelerate. Thus, the increase in the average coordination number of the DEM simulation causes its densification rate to increase and surpass that of the continuum calculation, revealing how particle rearrangement can significantly affect densification behavior.

The positive curvature of ρ with τ means that the densification rate $\dot{\rho}$ accelerates as ρ increases. In addition to the

contribution from particle rearrangement just noted, this behavior results from the linear dependence of the viscous and sintering parts of the normal force f^N on the contact radius a in Equation 1, combined with the increase of a with the length of particle overlap h (therefore ρ) according to Coble's geometric model of neck growth in Equation 3. This is in contrast with models for crystalline sintering limited by grain boundary diffusion, for which the viscous part is proportional to a^4 while the sintering part is constant (depending on $r\gamma$ instead of $a\gamma$).[27] While some evidence exists for an accelerating $\dot{\rho}$ at the onset of sintering,[2,47] the observed behavior of $\dot{\rho}$ in Figure 3 is generally inconsistent with experiments on viscous sintering, in which a deceleration is typically observed in the range of $0.6 < \rho < 0.9$.[48,49] However, the densification rates predicted by the model were shown by Jagota et al to be similar to those determined experimentally for the present range of relative density, justifying use of the model to probe sinter-cracking behavior. Nonetheless, future improvement of the model is warranted for a more realistic description of viscous sintering using DEM.

From a theoretical perspective, the corrected viscous sintering model of Frenkel, from which the sintering part of Equation 1 is derived and from which the accelerated $\dot{\rho}$ arises,[1] has been shown to give reasonable agreement with finite element analysis of the viscous sintering of two spheres.[39] For comparison with other sintering models, Figure 3 also shows the results of Mackenzie and Shuttleworth for a free-sintering viscous material made of closed spherical pores.[45] Although displaying a negative curvature, the Mackenzie-Shuttleworth model lies near the continuum average of Jagota et al and the present DEM results, predicting similar densification rates.

3.1.2 | Constrained sintering

In the case of constrained sintering, the specimen experiences macroscopic shrinkage in x and y only, while remaining intact in z. Figure 3 shows that the constrained specimen densifies more slowly than the free specimen, as expected due to a lack of shrinkage in z. The manner in which uniaxial restraint retards densification can be understood through a continuum analysis of the shrinkage of the constrained specimen. Following Bordia and co-workers,[2,50] we approximate the particle aggregate as an isotropic linear viscous compressible solid, in which the principal stresses (σ_i) and strain rates ($\dot{\varepsilon}_i$) are related as follows:

$$\begin{aligned}\dot{\varepsilon}_x &= \dot{\varepsilon}_f + \frac{\left[\sigma_x - N\left(\sigma_y + \sigma_z\right)\right]}{F},\\ \dot{\varepsilon}_y &= \dot{\varepsilon}_f + \frac{\left[\sigma_y - N\left(\sigma_z + \sigma_x\right)\right]}{F},\\ \dot{\varepsilon}_z &= \dot{\varepsilon}_f + \frac{\left[\sigma_z - N\left(\sigma_x + \sigma_y\right)\right]}{F}.\end{aligned} \tag{7}$$

The subscripts here refer to the directions of the principal stresses; N and F are Poisson's ratio and the viscous equivalent of Young's modulus (or the uniaxial viscosity) for a porous material and are both functions of ρ; $\dot{\varepsilon}_f$ is the free strain rate, which is experienced by the densifying material in the absence of external forces or constraints.

The boundary conditions for the constrained specimen are $\dot{\varepsilon}_z = 0$ and $\sigma_x = \sigma_y = 0$. The strain rates in the x and y directions are therefore.

$$\dot{\varepsilon}_x = \dot{\varepsilon}_y = \dot{\varepsilon}_f\left(1 + N\right). \tag{8}$$

Because Poisson's ratio for a sintering material is always positive,[50] Equation 8 predicts that the shrinkage rates in the directions transverse to the loading axis are faster in the constrained specimen than in the free specimen. This effect is confirmed by the simulations: at $\rho = 0.75$, the xy area of the constrained specimen is shrinking 7% faster than that of the free specimen.

The strain rate tensor, $\dot{\boldsymbol{\varepsilon}}$, is related to $\dot{\rho}$ by.

$$\frac{\dot{\rho}}{\rho} = -\mathrm{tr}\left(\dot{\boldsymbol{\varepsilon}}\right), \tag{9}$$

giving for the case of free sintering

$$\dot{\rho}_f = -3\rho\dot{\varepsilon}_f, \tag{10}$$

and for constrained sintering

$$\dot{\rho}_c = -2\rho\dot{\varepsilon}_f\left(1 + N\right). \tag{11}$$

Comparison of Equations 10 and 11 shows that $\dot{\rho}_c$ differs from $\dot{\rho}_f$ by a factor of $2(1 + N)/3$. The factor of 2/3 results from zero shrinkage in the z-direction while the term $(1 + N)$ reflects the enhanced x and y shrinkage rates due to Poisson's ratio.

To compare this result with the simulations, we use the expression for N developed by Scherer for a viscous sintering material with open porosity[51]:

$$N = \left(\frac{1}{2}\right)\left[\frac{\rho}{3 - 2\rho}\right]^{1/2}. \tag{12}$$

According to this expression, for $\rho = 0.75$, $N = 0.35$, thus the constrained specimen should be densifying 10% slower than the free specimen, in good agreement with the 14% observed for the simulations.

[1] In deriving the sintering part of f^N (second term in Equation 1), Jagota et al used a corrected form of Frenkel's model to describe the rate of change of the contact area due to sintering.[2] This model is compared with finite element analysis of the two sphere viscous sintering unit problem in Ref. [39].

3.2 | Stress evolution in the sintering specimen

Figure 4 shows the far-field tensile stress σ_{far} that developed in the densifying material as a function of the relative density ρ. The data are for specimens with an initial relative density ρ_0 of 0.70, an initial notch height b/H of 0.06, and the initial notch lengths d/W shown next to each curve. Here and in the next section, we focus on the unnotched specimen ($d/W = 0$).

At the onset of sintering, there is a transient stress (not shown) of 62 kPa due to an applied numeric force required to start the simulation. Following this initial transient, σ_{far} decreases to 43 kPa and then increases at a nearly constant rate as the specimen densifies. This far-field uniaxial stress can be converted to the sintering stress Σ using equations from viscous sintering theory:[50,51]

$$\Sigma = \frac{\sigma_{far}}{1-2N}, \tag{13}$$

where N is defined as in Equation 12. Thus for $\sigma_{far} = 43$ kPa at $\rho = 0.71$, following the transient, Equation 13 gives Σ to be 130 kPa. This is slightly larger but within an order of magnitude of the sintering stress determined experimentally for glass powders[48] and comparable with that predicted by theory for viscous sintering.[52] Furthermore, Rahaman and De Jonghe observed an increase in the sintering stress of borosilicate glass powder from 0.63 to 0.95 relative density,[48] in line with the behavior on display in Figure 4.

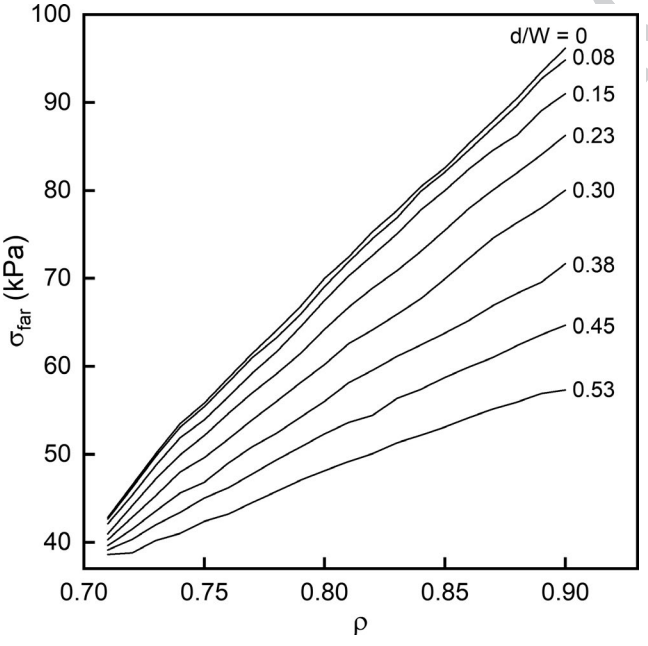

FIGURE 4 Far-field tensile stress σ_{far} plotted against the relative density ρ. σ_{far} is the average of stress values measured between the notches and the layers of fixed particles. A transient stress of 62 kPa at the onset of sintering has been omitted from all curves for clarity. Data are for a notch height b/H of 0.06 and the notch lengths d/W shown next to each curve

The positive slope of the stress evolution curves can be understood in terms of the normal force contact law, Equation 1. Macroscopically, the velocity term $\frac{dh}{dt}$ in Equation 1 is zero with respect to the z-direction because the fixed grip boundary conditions prevent vertical shrinkage. Hence, the tensile term containing the product of the contact radius a and the surface energy γ must give rise to the observed σ_{far} behavior. Because the surface energy is held constant during these simulations, there are only three potential contributions to the positive relationship between σ_{far} and ρ: (a) an increase in the mean radius of particle contacts with nonzero projected area in the z-direction, (b) an increase in the number density of such contacts, and (c) a decrease in the z-normal cross-sectional area caused by shrinkage transverse to the loading axis. The total z force (not shown) acting on the fixed particles increases in a manner similar to σ_{far}, suggesting that increase in the mean radius and number density of z-oriented particle contacts (resulting from particle rearrangement) causes the uniaxial stress to increase with time. This hypothesis is confirmed and discussed in Section 3.3.

The positive relationship between σ_{far} and the mean contact radius is further emphasized by comparing the initial sintering stress of specimens with different initial relative densities, which, because of the specimen preparation method, also had different initial mean contact radii. Unnotched specimens with ρ_0 values of 0.65, 0.70, and 0.75 had mean initial contact radii of 0.48, 0.87, and 1.11 μm, respectively; their initial σ_{far} values were 24, 43, and 60 kPa after the transient region. In each case, an increase in the initial contact radius gives a corresponding increase in the initial stress by approximately the same factor, demonstrating that the induced stress is a function of the contact size.

3.3 | Evolution of specimen anisotropy

Another effect of the uniaxial restraint is to induce development of an anisotropic structure in the specimen. To illustrate this point, Figure 5A is a polar histogram showing the angular distribution of particle contacts in the specimen, where the normal vectors for all contacts have been projected onto the yz plane. The histogram counts are normalized by the total number of particles so that integration of the curve gives the average coordination number: 7.1 at the start and 8.5 at the end of sintering from 0.70 to 0.90 relative density, revealing the creation of new particle contacts as a result of particle movement during densification. Prior to sintering, the distribution of contact orientation is isotropic; following densification, Figure 5A reveals that slight anisotropy has developed, with the creation of more contacts in z than in y.

COLOR online, B&W in print

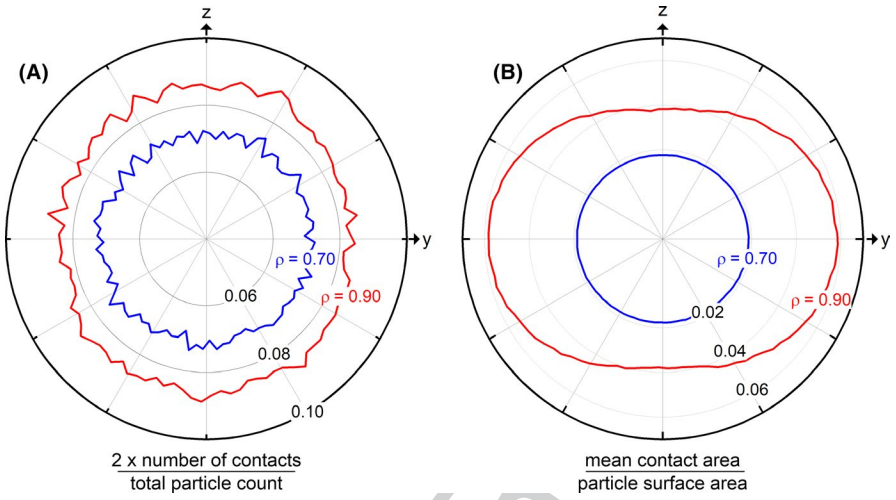

FIGURE 5 Angular distribution of (A) the average coordination number and (B) the mean contact area for the constrained unnotched specimen at the start of sintering (blue) and at the end of sintering (red). Relative densities ρ are indicated next to each curve. The graphs represent a projection of contact normal vectors onto the yz plane. Data are divided into 100 bins

COLOR online, B&W in print

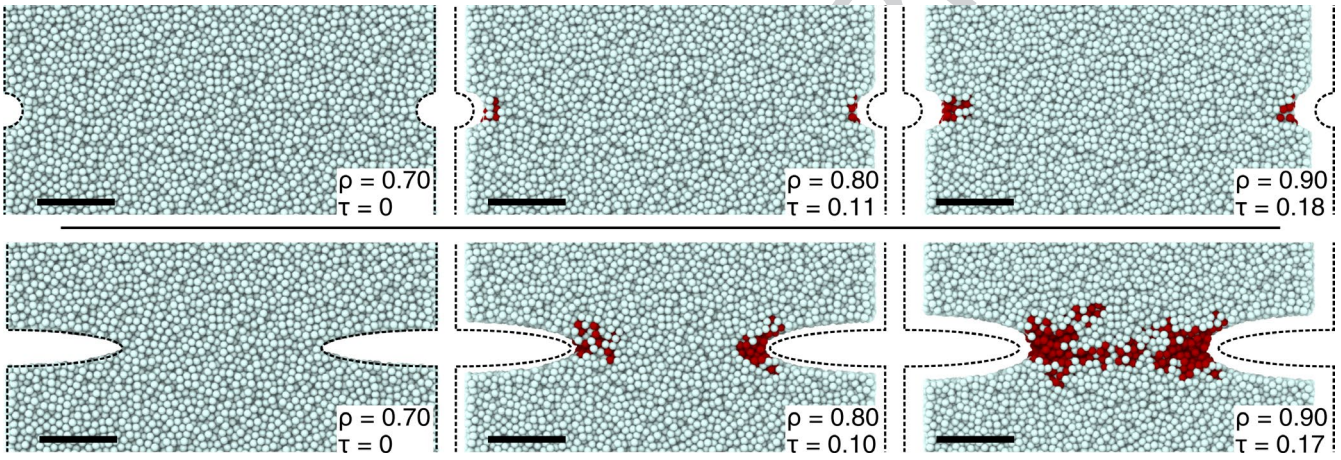

FIGURE 6 A shallow notch (3 particles deep, $d/W = 0.11$) and a deep notch (15 particles deep, $d/W = 0.56$) of the same height (5 particles, $b/H = 0.06$), shown at equal intervals of relative density ρ. Dark red particles represent cracks growing from the notch roots and the dashed lines indicate the initial specimen profile. Values of reduced time τ are shown. Scale bars are 50 μm

The anisotropic evolution of contact structure is even more obvious in Figure 5B, which shows the mean contact area normalized by the particle surface area. In Figure 5B, the contact size distribution begins as isotropic and then becomes strongly anisotropic as the specimen densifies, with the mean contact area normal to y growing 50% larger than that normal to z. Contact area growth in z is retarded by the vertical restraint, which prevents particles from coalescing in this dimension. However, the growth of contact area in z is still significant and must arise from particle rearrangement allowed by the random nature of the particle packing. Particle contacts oriented with nonzero components in both y and z can grow in size due to movement of the particles in y; likewise, movement of particles in y can lead to rotation of contacts toward z, thereby increasing contact area in z. The combined effect of this contact evolution is to increase σ_{far} in the constrained specimen, as shown by Figure 4.

3.4 | Effect of notch geometry on specimen behavior

3.4.1 | Microstructural evolution

We next consider the behavior of the specimens containing elliptical edge notches under constrained sintering conditions. As described in Section 2.5, the sinter-crack is defined as the continuous region of ruptured particle contacts emanating from the notch roots. While diffuse damage could be observed throughout the notched specimens, major cracking was confined to the regions adjacent to the notch roots.

Figure 6 shows a series of images taken at different stages of densification from 0.70 to 0.90 relative density for two types of notch geometries: shallow (length of 3 particles, $d/W = 0.11$) and deep (length of 15 particles, $d/W = 0.56$). Both notches have a height of 5 particles ($b/H = 0.06$),

corresponding to initial gross stress concentration factors of 3.5 and 15.6, respectively.[53] The dark red particles represent sinter-cracked material; the initial specimen profile is shown in each image.

The shallow notch specimen displays typical behavior for sintering under uniaxial restraint: its height remains constant while its width shrinks by 11% and its thickness by 14%, corresponding to a final relative density of 0.90. The shape of the notch changes slightly, widening in z by 17%. Crack growth begins early, proceeds gradually, and is confined to the region close to the notch, traveling a horizontal distance approximately equal to the notch length. A damage zone of separated particles accumulates adjacent to the notch root and expands vertically. The crack grows only slightly during densification from 0.80 to 0.90 relative density, and the final length of the crack developed by the shallow notch is 15% of the ligament width, far from complete fracture. Uncracked material between the notches resembles material far from the notches, indicating that the stress field around the sinter-cracks did not influence densification in the center of the specimen.

Like the shallow notch specimen, the deep notch specimen maintains a straight profile along its edges. However, it experiences less xy shrinkage than the shallow notch specimen (the width shrinking by 10% and the thickness by 13%). Less shrinkage in x and y indicates a contribution to densification from shrinkage in z—that is, less restraint on vertical displacement of particles—allowed by the greater length of the notches. As with the shallow notch, widening of the deep notch begins immediately but progresses much farther: at $\rho = 0.90$, the notch has widened by 70%. Crack growth begins immediately and proceeds rapidly, with large damage zones accumulating at the roots of the notches, expanding vertically and developing horizontal branches. At $\rho = 0.90$, the cracks have traveled completely through the ligament. The cracks do not grow far outside of the ligament region, demonstrating that damage tends to isolate between the defects, where stress concentration is greatest. Nevertheless, the sinter-cracking behavior observed here is more diffuse and less catastrophic than that observed in DEM simulations of crystalline material, where cracks easily traveled through the width of the specimen.[25]

We observe a tendency for particles to remain connected even when nearby particles have lost contact, producing crack-bridging ligaments that can slow crack growth. Similarly, Bordia and Jagota investigated sinter-crack propagation from a notch root in a glass powder film and observed connected particle ligaments bridging the crack opening.[9,20] Substantial crack-bridging behavior has also been observed in experiments using crystalline powders, where propagation of a sinter-crack from a notch was accompanied by sections of material connecting the two fracture surfaces.[9,21]

3.4.2 | Evolution of sinter-crack length

The behavior of sinter-cracks growing from the notches is demonstrated in Figure 7 by a plot of normalized crack length c/W vs ρ. The data are for a notch height of five particles ($b/H = 0.06$) and the full range of notch lengths tested. c was taken as the average length of the cracks growing from both notches. Normalization by W gives a sense of size with respect to the specimen.

In general, the sinter-cracks begin growing immediately and go through alternating phases of growth and arrest. For shallow notches of $d/W = 0.11$ and below (dashed lines in Figure 7), cracking is minimal and characterized by large regions of diminished growth or crack arrest. Continued densification of the specimen combined with the cessation of material rupture leads to shrinkage of the crack size during the arrest phases, a phenomenon recently observed experimentally through in situ monitoring of sinter-cracking in restrained notched panel specimens.[21] This behavior indicates a regime of notch geometry where catastrophic sinter-cracking is suppressed: while a crack may initiate, it will grow slowly or not at all.

In contrast to small notch lengths, notches larger than $d/W = 0.11$ display nearly linear increase of crack length with time, interrupted by short periods of crack arrest. These nongrowth regions may be incubation phases where the stress builds prior to overcoming the strength of the particle contacts; or, they may represent damage taking place ahead of the crack tip prior to linking with it. By inspecting the

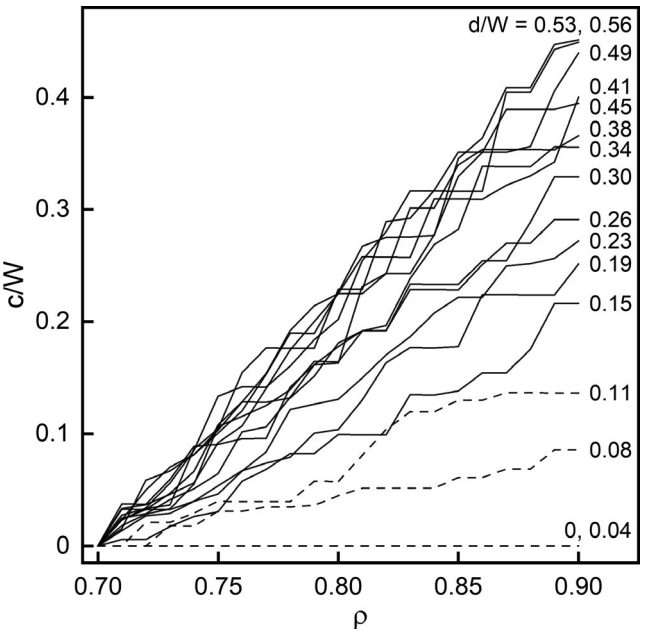

FIGURE 7 Crack length c normalized by specimen half-width W vs relative density ρ for a notch height b/H of 0.06 and ρ_0 of 0.70. Notch lengths d/W are shown next to each line. Dashed lines show large regions of little crack growth

sinter-cracking specimens, we find ligaments of connected material separating regions of damage; the sudden rupture of these ligaments leads to a jump in crack length. Such damage zone behavior was also observed in a sintering alumina film where the main sinter-crack grew by coalescing with voids that formed ahead of the crack.[9] It is also a common feature of creep-cracking in dense materials where crack growth occurs through the formation and coalescence of grain boundary cavities, sometimes accompanied by crack-bridging ligaments.[19,54]

As notch length increases to the maximum value tested, the crack length data become more closely spaced, indicating a limiting crack growth rate. Similar limiting behavior was found to apply to the mode I stress intensity factor (K_I) for a cracked sintering film: at first, K_I increases with the square root of the crack length, but then approaches a limiting value that is independent of crack length.[20] Finally, of all the notch lengths shown in Figure 7, only the greatest ($d/W = 0.56$) experiences cracking through the entire width of the internotch section.

Returning to Figure 4, the tensile stress experienced by the notched specimens may be understood in light of their cracking behavior. Data are shown for selected notch lengths ranging from $d/W = 0.08$ to 0.53 and an initial relative density of 0.70. For all notch lengths, the stress σ_{far} experienced by the notched specimen is less than that of the unnotched specimen, and as the length of the notch increases, σ_{far} decreases by greater amounts. This divergent behavior is a function of the competing processes of stress buildup through densification and stress relief through crack propagation. It also reflects the increase of specimen compliance due to the initial notch geometries and the growth of sinter-cracks from the notches.

3.4.3 | Densification between the notches

When cracking occurs, particle contacts at the notch root are broken by adjacent densifying material while unbroken particle contacts ahead of this cracked region continue to sinter. Densification continues ahead of the crack due to x and y shrinkage, which in turn strengthens the material against fracture. Shrinkage in these dimensions can also affect z-oriented contacts through particle rearrangement and contact rotation; such processes aid densification ahead of a stress-concentrator.[22]

Figure 8 shows the relative density measured far from the notches (far-field) and between the notches (internotch) for the two specimens shown in Figure 6 (shallow and deep notches). The reference spheres used for the measurement were the same initial size and were centered with respect to specimen thickness; their positions are indicated in the Figure 8 inset. For the shallow notch ($d/W = 0.11$), densification of far-field

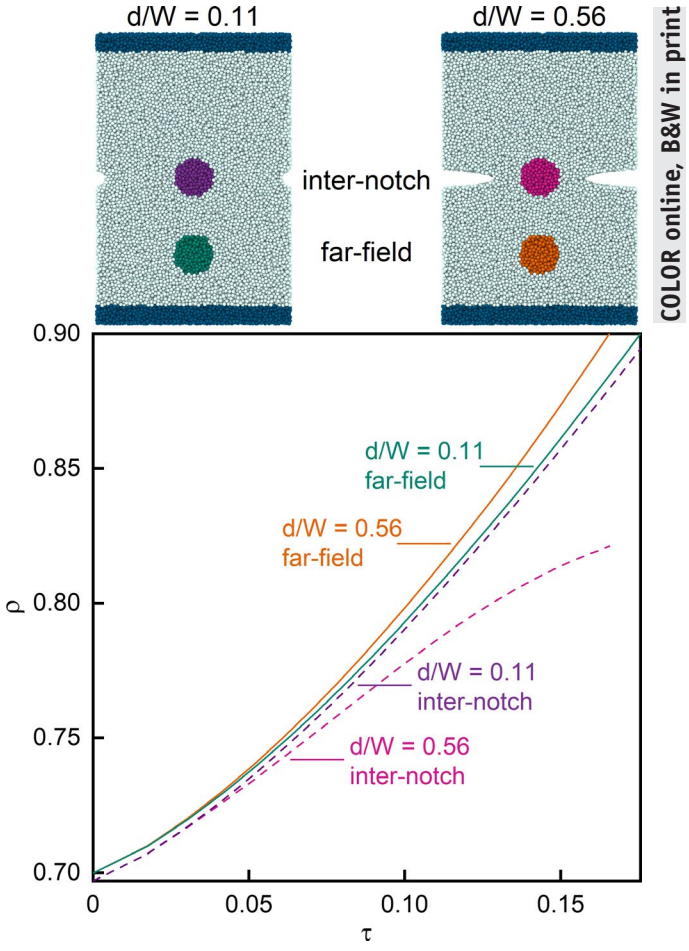

COLOR online, B&W in print

FIGURE 8 Relative density ρ plotted against reduced time τ for material far from the notches ('far-field', green and orange reference spheres) and between the notches ('internotch', purple and pink reference spheres). Data are for a notch height b/H of 0.06 and notch lengths d/W of 0.11 and 0.56

and internotch material is similar, indicating minimal effect due to the notches on microstructural evolution. For the deep notch ($d/W = 0.56$), densification behavior is similar at early stages, but diverges near a reduced time of 0.05. The far-field material begins to densify more rapidly due to a greater specimen compliance. Meanwhile, the internotch material continues densifying at a slower rate due to particle movement in x and y, even as desintering and contact rupture are taking place in z due to the concentrated stress near the notches.[55] A balance between these opposing processes, densification in x and y vs de-sintering in z, explains the crack arrest behavior observed for small notch lengths in Figure 7.

In their stress intensity analysis, Jagota and Hui determined a critical crack size for sinter-crack growth.[20] Similarly, for creep-cracking in fully dense materials, a threshold stress intensity factor has been identified below which cracks blunt and retract.[56] While we observed particle separation even for small notch lengths, crack growth was suppressed for notches below a certain size ($d/W \leq 0.11$, Figure 7). As

seen in Figure 8 for the shallow notch, densification ahead of the flaw progresses normally, supporting the critical crack size condition. In a similar stress intensity analysis, Ostertag et al suggested that suppression of crack nucleation is unlikely, while avoiding significant crack growth is of greater practical importance.[7] From Figure 8, the shallow notch shows this possibility: for a small enough flaw, densification of the bulk material is unaffected.

More generally, the gradients in structure and relative density that develop in the region between the notches can strongly influence the trajectory of the sinter-crack. The continued densification between the notches for the deep notch specimen suggests a material toughening mechanism that can serve to slow and potentially stop the growth of a sinter-crack. Even as the crack travels into the center of the specimen, x and y shrinkage continues to densify the material in the inter-notch region. Thus, crack arrest might result if densification ahead of the crack exceeds the tendency of the crack to grow.

3.5 | Fracture mechanics analysis of notched specimen behavior

3.5.1 | Specimen compliance

From linear elastic fracture mechanics, it is well-known that the compliance of a double edge notched specimen increases with the length of the notches and the length of cracks or damage emanating from them.[57,58] Furthermore, there is a mathematical analogy between linear elastic and linear viscous boundary value problems, which holds that solutions to linear elastic problems can be extended to identical linear viscous problems by replacing strains with strain rates and moduli with viscosities.[59] By applying this analogy to the linear elastic solution for the compliance of a cracked double edge notched specimen, we can determine the effect of the edge notches and sinter-cracks on the uniaxial stress observed in Figure 4.

For the specific constrained sintering problem that we are considering, the equivalent linear elastic boundary value problem is a linear thermoelastic panel with a positive coefficient of thermal expansion that is first restrained under fixed grip loading conditions at one temperature, then cooled to generate an internal tensile stress. The nondimensional load line compliance Z of this specimen is related to the induced thermal stress σ_{ind} through the Young's modulus E as follows:[57]

$$\sigma_{\text{ind}} = \frac{sEB}{ZA}, \tag{14}$$

where s is the displacement that would occur without the fixed grip conditions, B is the specimen thickness, and A is the cross-sectional area normal to the restraint. For thermoelastic shrinkage, the displacement s is determined by the linear thermal expansion coefficient α and change in temperature ΔT:

$$s = \alpha H \Delta T, \tag{15}$$

where H is the specimen height as in Figure 1. When the thermoelastic panel is cooled under fixed grip conditions, it experiences an induced stress according to Equations 14 and 15. The equations show that an increase in specimen compliance Z will produce a decrease in the stress σ_{ind} caused by a given change in temperature.

In the case of constrained sintering, the mass transport mechanisms that lead to densification are the cause of the induced stress. Following the linear viscous analogy, the displacement s is replaced by the displacement rate $\dot{s}$ and the Young's modulus E is replaced by the uniaxial viscosity F. As with the thermoelastic panel, $\dot{s}$ is the displacement rate which the densifying material would experience in the absence of external restraint and is therefore related to the free strain rate $\dot{\varepsilon}_f$ introduced in Section 3.1.2. Similar to the product $\alpha \Delta T$ for the thermoelastic case, $\dot{\varepsilon}_f$ represents the tendency of the specimen to shrink macroscopically and corresponds to the driving force for densification. For the case of uniaxial restraint, $\dot{s}$ is related to $\dot{\varepsilon}_f$ through the specimen height H aligned with the z restraining axis:

$$\dot{s} = \dot{\varepsilon}_f H. \tag{16}$$

For the constrained specimen, we determine $\dot{\varepsilon}_f$ from the densification measured by the reference sphere. The macroscopic strain rates $\dot{\varepsilon}_i$ are nominally zero in z due to the boundary conditions and approximately equal in x and y. Combining Equations 8 and 9 thus gives $\dot{\varepsilon}_f$ as.

$$\dot{\varepsilon}_f = \frac{\dot{\rho}}{2(1+N)\rho}, \tag{17}$$

where N is again the result of Scherer for Poisson's ratio of a viscous sintering material with open porosity.[51,60]

If the divergent stress behavior observed in Figure 4 is explained by the difference in specimen compliance, then the dependence of the uniaxial viscosity F on the relative density ρ should be similar for all specimens. Rearranging Equation 14, substituting Equations 16 and 17, and using σ_{far} instead of σ_{ind}, we obtain.

$$F = 2WZ\sigma_{\text{far}} \frac{2(1+N)\rho}{H\dot{\rho}}, \tag{18}$$

where we have replaced the instantaneous cross-sectional area A with the product of the instantaneous specimen dimensions B and $2W$.

For a double edge notched tension panel, Z is calculated by the following formula:[57]

Two lines

$$Z=\frac{H}{2W}+\frac{4}{\pi}\left\{0.0629-0.0610\left[\cos\left(\frac{\pi g}{2W}\right)\right]^4-0.0019\left[\cos\left(\frac{\pi g}{2W}\right)\right]^8+\ln\left[\sec\left(\frac{\pi g}{2W}\right)\right]\right\}, \tag{19}$$

where we define g as the sum of the notch length and one third of the crack length. This approximation compensates for the character of the sinter-crack: it is not a perfect through-thickness crack, to which Equation 19 applies, but instead tunnels through uncracked material as it grows from the notch. Further justification for this approximation is provided through a look at the stress profile in Section 3.7.

Figure 9 shows F plotted against ρ for the same notch lengths shown in Figure 4. For viscous sintering materials with open porosity, Scherer[60] has used a thermoelastic analysis to approximate the uniaxial viscosity as.

$$F=\frac{3\eta\rho}{3-2\rho}. \tag{20}$$

The evolution of F during sintering seen in Figure 9 is in qualitative agreement with that predicted by Scherer for late sintering densities ($\rho > 0.75$), the curves lying parallel to each other. The values from Scherer in this range are less than those of the unnotched specimen, revealing the difference between the model due to Scherer, which is based on porosity as a state variable, and the model due to Jagota et al used in our simulations, which is based on particle contacts. Unlike the stress in Figure 4, which showed divergent behavior for the different notch lengths as sintering progressed, the uniaxial viscosity curves lie parallel to each other beyond $\rho = 0.75$, showing similar evolution of F with ρ and indicating that change in specimen compliance is an important factor in the change of the measured far-field stress. The spread seen at the early stages of sintering in Figure 9 is caused by delay in the distribution of stress through the material at the onset of sintering. As sintering progresses, the stress distributes throughout the specimen and the viscosity curves converge.

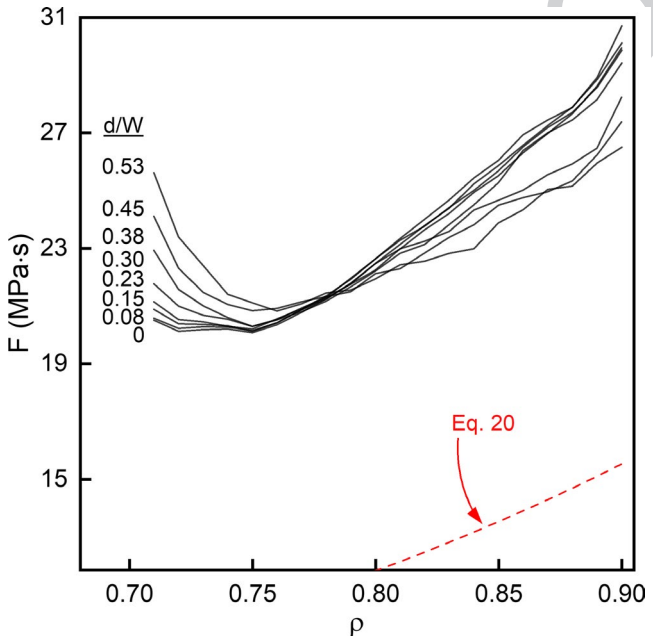

FIGURE 9 Uniaxial viscosity F, as calculated from the specimen compliance, plotted against the relative density ρ. Data are for specimens of initial relative density 0.70, notch height b/H of 0.06, and normalized notch lengths d/W shown next to the curves. The data points corresponding to the initial stress transient have been omitted. The red dashed line is Scherer's approximation[60]

From a practical perspective, it is common in experimental fracture mechanics to determine the length of a crack in a specimen based on the measured load line compliance. The present results suggest that this method can be used to determine the length of sinter-cracks as well, provided the densification kinetics are known. Finally, it is apparent that the presence of a notch allows far-field densification to occur more rapidly. As seen in the measurements of far-field relative density in Figure 8, the deep notch specimen ($d/W = 0.56$) attains $\rho = 0.90$ at a lower reduced time than the shallow notch specimen ($d/W = 0.11$). This faster densification is the result of less restraint on the far-field material due to the notches and the sinter-cracks, which increase the specimen compliance.

3.5.2 | Dependence of cracking behavior on notch geometry

There are a variety of candidate parameters that might be used to describe the stress field ahead of a sinter-crack, including the stress concentration factor,[61] stress intensity factor,[57] creep-crack growth parameter C^*,[19] and net section stress.[62] If the stress field can be calculated accurately, then cracking behavior may be predicted. To test the relevance of these parameters to sinter-cracking, we simulated a range of notch heights and lengths, then compared the extent of sinter-crack growth with different parameters representing the initial specimen geometry.

The gross stress concentration factor K_{tg} can represent the effect of both the height and length of the notch and is typically used for discontinuities that are not atomically sharp. For opposing elliptical edge notches in a symmetrical panel, K_{tg} is given by[53]

2 lines

$$K_{tg}=\left(0.855+2.21\sqrt{d/q}\right)\left[1-0.50\left(\frac{d}{W}\right)-0.0134\left(\frac{d}{W}\right)^2+0.081\left(\frac{d}{W}\right)^3\right]\left[1-\frac{d}{W}\right]^{-1/2}, \tag{21}$$

where q is the radius of curvature of the notch root, a function of both the height and length of the notch, and d and W are

as defined in Figure 1. We calculate K_{tg} for each initial specimen geometry and compare it with the final normalized crack length c/W after sintering from 0.70 to 0.90 relative density. The data are plotted in Figure 10A for all notch heights and lengths considered. As expected, a greater K_{tg} produces a greater final crack length. However, there is significant spread between the curves and specific values of K_{tg} do not predict unique final crack lengths, demonstrating that K_{tg} is not a good descriptor of sinter-crack growth in this case.

This result was also obtained in an experimental study on creep rupture of fully dense copper and aluminum, where it was found that creep rupture did not depend on the stress concentration factor and did not vary with the height of the flaw.[62] Instead, there was a correlation between rupture life and a normalized representative rupture stress, a quantity composed of the average stress acting on the minimum section adjacent to the flaw and the uniaxial creep rupture data for the material. Accordingly, we test the influence of the minimum section on sinter-cracking behavior by plotting c/W against the initial normalized notch length d/W in Figure 10B. Except for some slight deviations, the results for different notch heights overlap for the entire range of d/W. The final crack length generally increases with the initial length of the notch, but plateaus at higher values of d/W, revealing again the limiting dependence of crack growth on flaw size seen in the plots of crack length vs relative density in Figure 7.

Figure 10 demonstrates that cracking behavior depends strongly on the initial length of the notch, with no obvious contribution from its height for those values tested. This result is counter to intuition, since in a nonporous material with an externally applied stress, the K_{tg} of the notch should influence cracking behavior by having a multiplying effect on the crack tip stress field after the crack has initiated.[63] Its lack of influence in this case may be due to the small difference between particle and notch size, so that even nominally blunt notches behave as sharp cracks. Another possible explanation is that although the notch root may have a large macroscopic radius of curvature, the interparticle necks at the notch root have a radius of curvature orders of magnitude smaller, so that the interparticle necks act as sharp crack tips; this is consistent with theory for porous materials, for which mechanical properties are expected to depend on the stress concentration factor of the pores.[64] Nevertheless, the correlation between the final crack length and initial notch length strongly suggests the use of stress parameters that depend on the flaw length only, such as the stress intensity factor, creep-crack parameter, or net section stress.

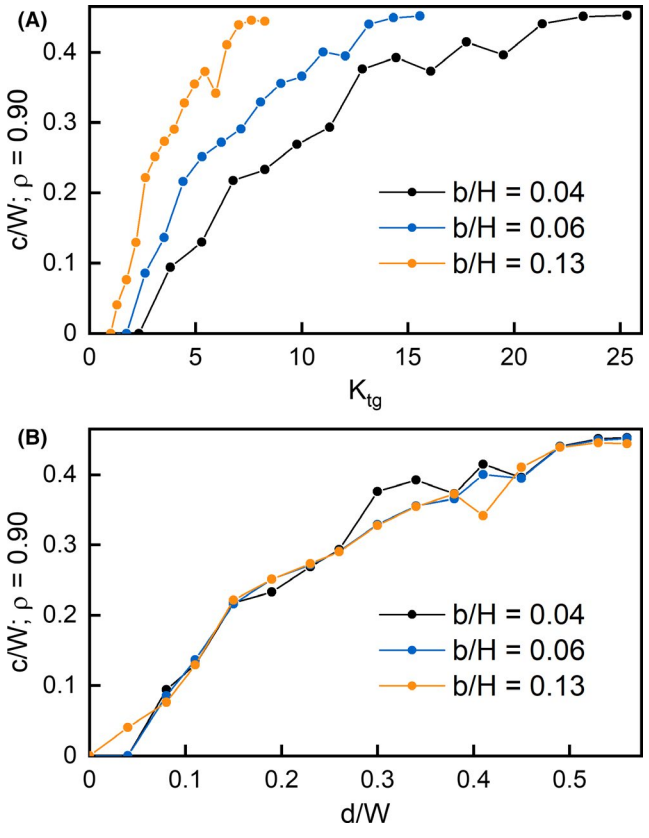

FIGURE 10 Final normalized crack length c/W plotted against (A) the initial stress concentration factor K_{tg} and (B) the initial normalized notch length d/W for specimens sintered from $\rho = 0.70$ to 0.90. All notch heights and lengths are shown

3.6 | Effect of initial relative density on crack growth

Multiple investigators have considered the dependence of sinter-cracking behavior on the initial relative density ρ_0 of powder aggregates and have arrived at conflicting conclusions. Some found that sinter-crack growth was more rapid in specimens with low ρ_0.[7] Others found that sinter-crack growth was more rapid for greater ρ_0 because particle rearrangement, an important energy dissipation and stress relaxation mechanism, is suppressed at higher relative densities.[15,25]

To shed light on the effect of ρ_0, sinter-cracking behaviors are compared in a plot of normalized crack length c/W vs initial normalized notch length d/W in Figure 11 for specimens of constant notch height and different ρ_0. c/W was measured at a reduced time τ of 0.1 for even comparison of specimens with different ρ_0. Figure 11 shows that, for nearly all values of d/W, c/W decreases with ρ_0. For $d/W = 0.3$ and $\rho_0 = 0.65$, the crack length at $\tau = 0.1$ is $2x$ that of $\rho_0 = 0.70$ and $4x$ that of $\rho_0 = 0.75$. It is interesting to note that the uniaxial stress alone is not a predictor of cracking behavior: as mentioned in Section 3.2, specimens with greater ρ_0 experienced greater far-field stress, but here exhibit lower crack growth rates.

The ρ_0 dependence evident in Figure 11 is opposite that found in DEM simulations of cracking in crystalline materials sintered under similar conditions (notched panel, uniaxial restraint).[25] There, complete fracture was observed for

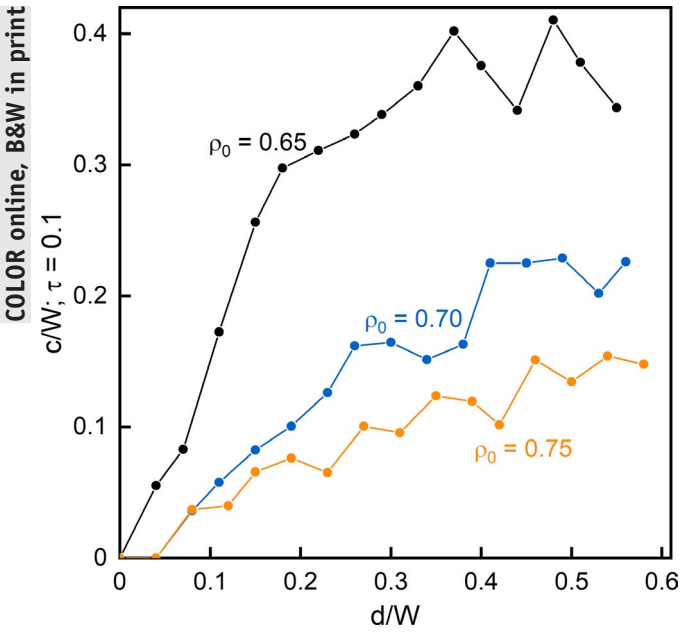

FIGURE 11 Normalized crack length c/W vs initial normalized notch length d/W for different initial relative densities ρ_0 and a notch height b/H of 0.06. Crack lengths were measured at a reduced time τ of 0.1

higher ρ_0, while for lower ρ_0, more cracks initiated and crack opening was greater, but complete fracture did not occur. Thus, the resistance to sinter-cracking in crystalline powder aggregates appears to increase with decreasing ρ_0. Martin et al attributed this effect to the higher viscosity of the denser aggregate, which reflects the larger mean contact radius and higher particle coordination number associated with higher relative density, and the stronger dependence of the aggregate viscosity on the contact radius for a crystalline material. These factors inhibit particle rearrangement and other stress relaxation mechanisms at the crack tip, thus promoting fracture.

The results shown in Figure 11 also suggest that viscosity influences sinter-cracking behavior, since the viscosities of the glass powder aggregates scale with relative density, as seen in Figure 9. However, in the present case of a glass material, our results indicate that a lower viscosity leads to a greater crack growth rate. This inverse dependence of crack growth rate on viscosity has also been observed for creep-cracking in fully dense materials, including polycrystalline ceramics, where the phenomenon, referred to as Monkman-Grant behavior, has been associated with diffusion-mediated cavitation ahead of the crack.[65,66] Other investigations have identified an inverse dependence of creep-crack growth rate on cavity spacing, a parameter analogous to the relative density.[58,67] Thus, the parallel behavior between creep-cracking and sinter-cracking observed here further supports the analogy between the two processes. While this conclusion differs from the sinter-crack behavior found in simulations of crystalline materials, we note that it matches what has been observed experimentally in sintering aggregates of MgO, where higher crack opening and displacement velocities were associated with lower ρ_0 for the aggregates, corresponding to lower aggregate viscosities.[7]

3.7 | The stress profile between the notches

From the force vectors acting on particle contacts and the corresponding particle center-to-center position vectors, the local stress tensor $\boldsymbol{\sigma}$ is calculated for each particle in the system using Equation 5. The zz component of $\boldsymbol{\sigma}$, σ_{loc}, is shown for particles in the notch region as a function of y-position in Figure 12 over the course of sintering from 0.70 to 0.90 relative density. The notch region is defined for particles with absolute z-position less than 30 μm and absolute x-position less than 5 μm. The instantaneous positions of the notch and crack tips are represented in Figure 12 by vertical solid and dashed lines, respectively. Above each graph is a contour map showing the σ_{ave} stress field and a rendering showing the cracked material. The contour maps show that far from the notches, the tensile stress is nearly uniform across the width of the specimen. Between the notches, the stress is amplified in a lobe pattern that expands as the specimen densifies, with the greatest stress lying ahead of the notch tips.

The stress data σ_{loc} show a relatively uniform tensile stress experienced by particles lying between the crack tips, increasing on average as the specimen densifies. Ahead of the notch and behind the crack tip, particles experience greater σ_{loc} due to stress concentration from the notch, while behind the notch tip σ_{loc} decays toward zero due to the free surface of the notch. Many values of σ_{loc} lie above 100 kPa, representing local stress concentration effects that cause an increase over the far-field stress values observed in Figure 4. During densification, σ_{loc} tends to increase until a cracking event (particle separation) takes place, after which it sharply decreases. The position of these local maxima between the notch and crack tips justifies the use of the crack length approximation in Equation 19. While the crack tip represents the farthest extent of particle contact rupture, the region of greatest stress concentration lies behind the tip, where a greater amount of contact rupture has occurred, extending more completely through the thickness of the specimen.

Superimposed on σ_{loc} is the continuous average stress profile $\overline{\sigma}$, calculated from σ_{loc} by the spatial averaging method described in Section 2.4. The graphs in Figure 12 show that $\overline{\sigma}$ tracks the behavior of σ_{loc}, exhibiting a uniform stress between the crack tips and stress amplification near the notches. As discussed in Section 3.2, the magnitude of the stress observed here is consistent with that observed experimentally for glass powders[48] and that determined theoretically for viscous sintering.[52]

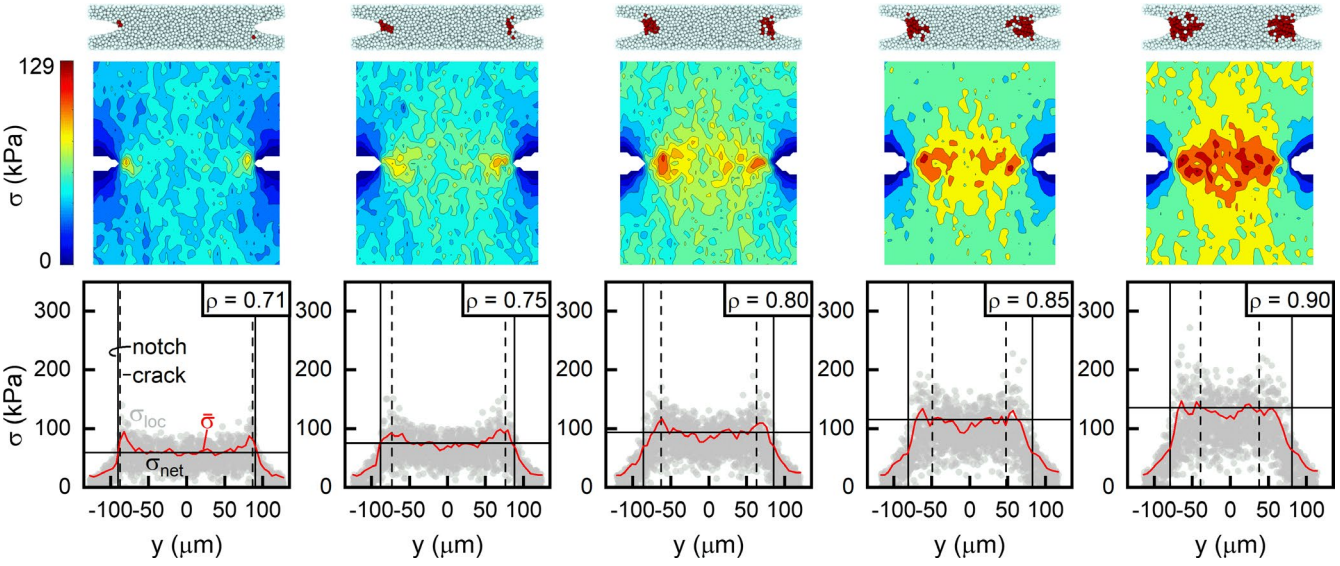

FIGURE 12 Stress profiles (bottom row) showing tensile stress σ in the notch region as a function of y-position: σ_{loc} is the zz component of individual particle stress tensors; $\overline{\sigma}$ is the mean profile determined by spatial averaging over the region; σ_{net} is the net section stress acting on the material between the notches. Vertical solid lines show the positions of the notch tips and vertical dashed lines show the positions of the crack tips. Instantaneous relative densities are given in the top right of each graph. Data are for $\rho_0 = 0.70$, $b/H = 0.06$, $d/W = 0.34$, and particles in the region $|z| < 30$ μm and $|x| < 5$ μm. Above each graph is the corresponding σ_{ave} stress field shown as a contour map. Renderings of the sinter-cracks are shown at the top

$\overline{\sigma}$ also reveals stress relaxation during densification. Initially, $\overline{\sigma}$ displays pronounced maxima near the notch tips, consistent with findings of finite element analysis for different types of heterogeneities in constrained sintering materials.[7,26] As densification proceeds, these maxima diminish, and the stress profile between the notches assumes a uniform value characterized by the net section stress σ_{net}:[67]

$$\sigma_{net} = \frac{2W\sigma_{far}}{(2W - 2g)}, \tag{22}$$

where g is the median crack length as in Equation 19. σ_{net} represents the average stress acting on the minimum cross section of the specimen and is shown as a horizontal black line in each graph of Figure 12.[62] It lies alongside $\overline{\sigma}$ between the crack tips and shows good agreement with the stress profile in this region.

This result is indicative of a creeping material in which the initial elastic stress field ahead of a stress concentrator is relaxed through creep deformation at elevated temperatures and low applied loads.[65,67] In the sinter-cracking specimen, the stress field resembles the elastic case at the start of densification, before significant deformation has occurred. Then, particle rearrangement and contact rupture cause the stress in this region to relax to the net section value. Thus, Figure 12 shows that a far-field stress measurement may be used to evaluate the stress field between the notches, a valuable result for experimental work. To our knowledge, this is the first quantitative view of the stress profile ahead of a flaw in a sinter-cracking specimen that does not depend on continuum approximations.

The large local values of σ_{loc} that lie between the notch and crack tips reveal the presence of uncracked material in the region. The sinter-crack does not propagate as a through-thickness crack, but in a diffuse manner, leaving unbroken particle contacts in its wake. Stress from the densifying far-field material continues to act on these connected particles, and local stress concentration from the notch leads to large values of σ_{loc} prior to further rupture. This crack bridging behavior has been observed as ligaments bridging fracture surfaces in fully dense creep-cracking materials, such as ceramics containing an amorphous phase, causing a decrease in the stress felt by the material at the crack tip.[68] However, damage is not limited to the region within the crack. Ahead of the crack tip, particle separation occurs prior to linking with the main crack. Such events are evidenced by local maxima in σ_{loc} lying ahead of the crack tips in Figure 12, and they form a damage zone through which the crack propagates. In fully dense creep-cracking materials, the formation of grain boundary cavities ahead of the crack tip by creep deformation causes a damage zone which weakens the material and promotes crack propagation.[58] In such a system, crack growth behavior is dependent on the spacing of the cavities.[67] We expect that sinter-cracking will have a similar dependence on the distance between broken particle contacts.

3.8 | Correlation of the crack growth rate with stress

To determine the relation between crack growth behavior and the stress induced by densification, it is helpful to look at the phenomenon of creep-cracking, to which sinter-cracking has been likened by others and to which the present results suggest a strong similarity.[7,9,21] Clear similarities exist between the two phenomena, including the time-dependent flow of material, cracking under small stresses, and rupture by intergranular failure.[19,67] In creep-crack growth, investigators have observed correlations between the crack growth rate $\dot{c}$ and some power of the stress intensity factor K_I^n or the net section stress σ_{net}^n, where n is often equal to the stress exponent in the creep rate deformation law.[67] Dependence on K_I^n has been attributed to creep brittle materials and high applied stresses, while dependence on σ_{net}^n has been attributed to creep ductile materials and low applied stresses.[67,69] The stress profiles in Figure 12 reveal that σ_{net} characterizes the stress in the region between the notches where cracking occurs, and that elastic parameters such as K_I do not apply due to stress relaxation. The sinter-cracking specimens experience low applied stresses (Figure 4) and the high strains involved in densification imply ductile material behavior (Figure 3), suggesting the application of σ_{net}. It has been further observed for fully dense materials that creep rupture behavior depending on σ_{net} is indifferent to the elastic stress concentration factor,[62] as observed here for sinter-cracking (Figure 10).

To test for a correlation between $\dot{c}$ and σ_{net}, we calculate the instantaneous sinter-crack growth rate $\dot{c}$ at densification intervals of 0.01 for all notch heights and lengths described in Section 2.1, discarding small negative changes in crack size caused by shrinkage of the specimen. The corresponding σ_{net} values are calculated according to Equation 22 and the results are plotted in Figure 13. The correlation between $\dot{c}$ and σ_{net} is good, with most values of $\dot{c}$ lying between 10^{-7} and 10^{-5} m/s, suggesting that the two quantities are related through a power law of the form $\dot{c} \propto \sigma_{net}^n$. Dependence of $\dot{c}$ on σ_{net} in creep rupture of fully dense materials has been attributed to creep relaxation of the stress field via viscous flow or diffusion.[56,70,71] In the case of sinter-cracking, stress relaxation can also result from particle rearrangement.[22] A minor group of data points falls at low values of $\dot{c}$, below 10^{-7} m/s. These points represent the competing processes that tend to suppress advancement of the crack, such as particle rearrangement and contact growth taking place ahead of the crack tip, as well as overall shrinkage of the specimen.

The observed crack growth rate is on the order of μm/s for a σ_{net} of ~ 100 kPa, a rate greater than the 0.1 μm/s crack growth rate observed through experiment for a

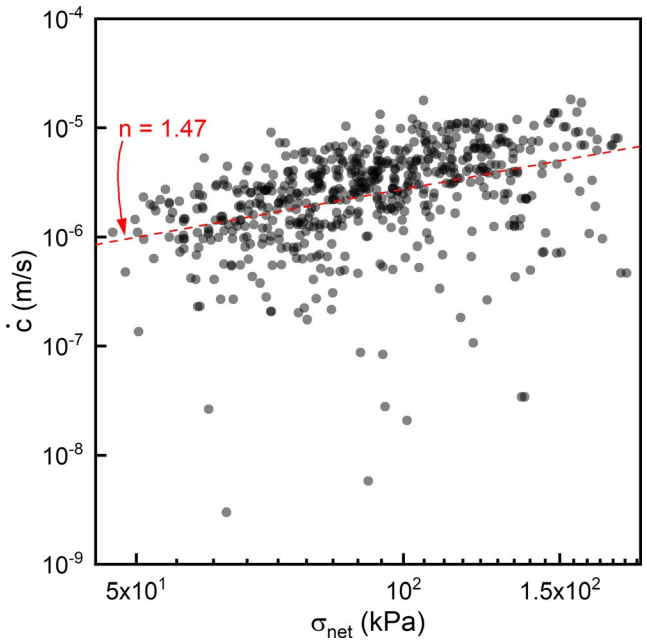

FIGURE 13 Rate of sinter-crack growth with respect to time $\dot{c}$ plotted against the net section stress σ_{net}. Data are for specimens of initial relative density 0.70 and all notch heights and lengths tested. The red dashed line is a linear regression fit of the data with slope n shown

crystalline material densifying more slowly.[21] A linear regression fit of the log-log data gives n as 1.47 ± 0.14, close to the value of 1 for a linear viscous material. This value is consistent with that expected for a sintering material, which is classically approximated as linear viscous.[50,72] The result is also consistent with the dependence expected for a model of crack velocity based on viscous flow.[70] For comparison, K_I was calculated[2] using the same median crack length g and far-field stress σ_{far} as for σ_{net}. The resulting plot of $\dot{c}$ vs K_I is given in the Supplementary Material along with the stress profiles predicted by K_I for the specimen shown in Figure 12. While a correlation between $\dot{c}$ and K_I can also be observed, the stress profiles in Figure 12 reveal that the physically meaningful description is based on σ_{net}.

The stress relaxation behavior seen in Figure 12 and the correlation between $\dot{c}$ and σ_{net} demonstrated in Figure 13 shed new light on recent observations of sinter-cracking. Complex phenomena such as the existence of a crack incubation phase and phases of crack arrest and shrinkage can be explained in terms of particle rearrangement, crack-bridging, and transverse shrinkage of the constrained sintering material.[21] Contrary to previous analyses,[7,17,20] the stress field in a sinter-cracking material is not found to depend on elastic stress parameters, such as the stress concentration factor or

[2] K_I for a double edge notched tension specimen was used.[57] The formula is given in the Supplementary Material.

stress intensity factor, but instead shows consistency with ductile creep-cracking behavior. While crack initiation in the presence of a stress-concentrator is likely, the present simulations show the probability of a threshold flaw size below which sinter-cracking is significantly mitigated. On a practical note, the dependence of the sinter-crack growth rate on the net section stress implies a failure criterion based on the minimum section of material, which could aid in the design of sinter-crack–resistant structures.

4 | CONCLUSIONS

We have investigated the cracking behavior of edge notched powder aggregates sintered under uniaxial restraint. Through a detailed analysis of densification, stress evolution, and cracking behavior, we reach the following conclusions:

1. Restraint retards densification of the powder aggregate; however, linear shrinkage is accelerated in dimensions perpendicular to the restraint because the effective Poisson's ratio of a sintering material is positive.
2. Restraint causes stresses to develop in the sintering aggregate, arising ultimately from the surface energy of the material. The introduction of flaws, such as edge notches, aligned perpendicular to the induced stress causes the far-field internal stress to decrease, an effect that can be described on the basis of specimen compliance, with greater flaw size leading to a greater specimen compliance and a decreased far-field stress.
3. The presence of flaws concentrates the internal stress and leads to the initiation of cracks. Cracks initiating at the flaws exhibit intermittent growth, characterized by alternating periods of arrest and advance. This behavior results from crack-bridging ligaments and continued densification ahead of the crack. There appears to be a critical flaw size below which crack growth is limited and experiences prolonged arrest; above this critical flaw size, crack growth is nearly continuous. For large initial flaws, the crack growth rate reaches a limiting value, as predicted by stress intensity analysis of a sinter-crack in a thin film sintered on a rigid substrate.[20]
4. The stress field in the powder aggregate is best described by the net section stress, rather than parameters such as the stress concentration factor or stress intensity factor. By comparing the crack growth rate with the net section stress, a correlation is found that is consistent with observations in the creep-cracking literature. The present results show that the crack growth rate is linearly proportional to the net section stress, supporting the classical approximation of a sintering material as linear viscous.
5. Greater crack growth rates are observed for specimens of lower initial relative density, due to their lower effective viscosity. Lower effective viscosity allows greater crack tip velocity, as observed in previous sinter-cracking experiments.[7] Thus, to suppress sinter-cracking in a powder aggregate, a greater green density is desirable.
6. The stress field in a constrained sintering material is affected by flaw size and by stress relaxation due to creep and particle rearrangement. For sufficiently small flaws, the stress field is small and material ahead of the flaw densifies normally. For larger flaws, densification ahead of the flaw decelerates but still takes place due to shrinkage perpendicular to the restraint. In both cases, relaxation of the stress field near the flaws is expected due to creep deformation of the material. Taken together, these mechanisms are expected to contribute to crack mitigation or arrest.

ACKNOWLEDGMENTS

We gratefully acknowledge Rice University and the National Science Foundation, project number NSF-CMMI-1826064, for financial support of this work. It is our pleasure to acknowledge Prof. Hesam Askari of the University of Rochester, for helpful discussions on relating discrete and continuous stress phenomena, and Ms Lynnora Grant of Rice University, for helpful discussions on the evolution of sintering contacts.

ORCID

Joseph R. Carazzone https://orcid.org/0000-0003-2387-2349
Zachary C. Cordero https://orcid.org/0000-0002-2578-3836
Christophe L. Martin https://orcid.org/0000-0002-9718-826X

REFERENCES

1. Wakai F, Katsura K, Kanchika S, Shinoda Y, Akatsu T, Shinagawa K. Sintering force behind the viscous sintering of two particles. Acta Mater. 2016;109:292–9.
2. Jagota A, Mikeska KR, Bordia RK. Isotropic constitutive model for sintering particle packings. J Am Ceram Soc. 1990;73(8):2266–73.
3. Ashby MF. A first report on sintering diagrams. Acta Metall. 1974;22(3):275–89.
4. Swinkels FB, Ashby MF. A second report on sintering diagrams. Acta Metall. 1981;29(2):259–81.
5. Jagota A, Hui CY. Mechanics of sintering thin films — I. Formulation and analytical results. Mech Mater. 1990;9(2):107–19.
6. Sudre O, Bao G, Fan B, Lange FF, Evans AG. Effect of inclusions on densification: II, Numerical model. J Am Ceram Soc. 1992;75(3):525–31.
7. Ostertag CP, Charalambides PG, Evans AG. Observations and analysis of sintering damage. Acta Metall. 1989;37(7):2077–84.
8. Cheng T, Raj R. Flaw generation during constrained sintering of metal-ceramic and metal–glass multilayer films. J Am Ceram Soc. 1989;72(9):1649–55.
9. Bordia RK, Jagota A. Crack growth and damage in constrained sintering films. J Am Ceram Soc. 1993;76(10):2475–85.
10. Lange FF. Densification of powder rings constrained by dense cylindrical cores. Acta Metall. 1989;37(2):697–704.
11. Cai PZ, Green DJ, Messing GL. Constrained densification of alumina/zirconia hybrid laminates, I: experimental observations of processing defects. J Am Ceram Soc. 1997;80(8):1929–39.

12. Maximenko AL, Van Der Biest O. Modelling of damage development during sintering. J Eur Ceram Soc. 2001;21(8):1061–71.
13. Lange FF, Metcalf M. Processing-related fracture origins: II, Agglomerate motion and cracklike internal surfaces caused by differential sintering. J Am Ceram Soc. 1983;66(6):398–406.
14. Sudre O, Lange FF. Effect of inclusions on densification: I, Microstructural development in an Al_2O_3 matrix containing a high volume fraction of ZrO_2 inclusions. J Am Ceram Soc. 1992;75(3):519–24.
15. Li F, Pan J, Cocks A. Defect healing and cracking in ceramic films during constrained sintering. J Am Ceram Soc. 2012;95(12):3743–9.
16. Hsueh CH, Evans AG, Cannon RM, Brook RJ. Viscoelastic stresses and sintering damage in heterogeneous powder compacts. Acta Metall. 1986;34(5):927–36.
17. Sglavo VM, Cai PZ, Green DJ. Damage in Al_2O_3 sintering compacts under very low tensile stress. J Mater Sci Lett. 1999;18(11):895–900.
18. Wang X, Atkinson A. Microstructure evolution in thin zirconia films: experimental observation and modelling. Acta Mater. 2011;59(6):2514–25.
19. Riedel H. Creep crack growth. In: Wei RP, Gangloff RP, editors. Fracture mechanics: perspectives and directions (Twentieth Symposium). Philadelphia, PA: American Society for Testing and Materials; 1989. p. 101–26.
20. Jagota A, Hui CY. Mechanics of sintering thin films — II. Cracking due to self-stress. Mech Mater. 1991;11(3):221–34.
21. Carazzone JR, Bonar MD, Baring HW, Cantu MA, Cordero ZC. In situ observations of cracking in constrained sintering. J Am Ceram Soc. 2019;102(2):602–10.
22. Henrich B, Wonisch A, Kraft T, Moseler M, Riedel H. Simulations of the influence of rearrangement during sintering. Acta Mater. 2007;55(2):753–62.
23. Jauffrès D, Martin CL, Bordia RK. Design of strain tolerant porous microstructures – a case for controlled imperfection. Acta Mater. 2018;148:193–201.
24. Lichtner A, Roussel D, Röhrens D, Jauffres D, Villanova J, Martin CL, et al. Anisotropic sintering behavior of freeze-cast ceramics by optical dilatometry and discrete-element simulations. Acta Mater. 2018;155:343–9.
25. Martin CL, Camacho-Montes H, Olmos L, Bouvard D, Bordia RK. Evolution of defects during sintering: discrete element simulations. J Am Ceram Soc. 2009;92(7):1435–41.
26. Rasp T, Jamin C, Guillon O, Kraft T. Cracking and shape deformation of cylindrical cavities during constrained sintering. J Eur Ceram Soc. 2017;37(8):2907–17.
27. Martin CL, Schneider LCR, Olmos L, Bouvard D. Discrete element modeling of metallic powder sintering. Scr Mater. 2006;55(5):425–8.
28. Martin CL, Bouvard D, Shima S. Study of particle rearrangement during powder compaction by the discrete element method. J Mech Phys Solids. 2003;51(4):667–93.
29. Stukowski A. Visualization and analysis of atomistic simulation data with OVITO–the Open Visualization Tool. Modelling Simul Mater Sci Eng. 2010;18(1):015012.
30. Martin CL, Bordia RK. The effect of a substrate on the sintering of constrained films. Acta Mater. 2009;57(2):549–58.
31. Mercadelli E, Montaleone D, Gondolini A, Pinasco P, Sanson A. Tape-cast asymmetric membranes for hydrogen separation. Ceram Int. 2017;43(11):8010–7.
32. Mücke R, Menzler NH, Buchkremer HP, Stöver D. Cofiring of thin zirconia films during SOFC manufacturing. J Am Ceram Soc. 2009;92:S95–S102.
33. Carpanese MP, Barbucci A, Canu G, Viviani M. $BaCe_{0.85}Y_{0.15}O_{2.925}$ dense layer by wet powder spraying as electrolyte for SOFC/SOEC applications. Solid State Ionics. 2015;269:80–5.
34. Jagota A, Scherer GW. Viscosities and sintering rates of composite packings of spheres. J Am Ceram Soc. 1995;78(3):521–8.
35. Bordia RK, Kang S-JL, Olevsky EA. Current understanding and future research directions at the onset of the next century of sintering science and technology. J Am Ceram Soc. 2017;100(6):2314–52.
36. Coble RL. Initial sintering of alumina and hematite. J Am Ceram Soc. 1958;41(2):55–62.
37. Jagota A, Dawson PR. Simulation of the viscous sintering of two particles. J Am Ceram Soc. 1990;73(1):173–7.
38. McLellan GW, Shand EB. Glass engineering handbook, 3rd edn. New York, NY: McGraw-Hill; 1984.
39. Jagota A, Dawson PR. Micromechanical modeling of powder compacts—I. Unit problems for sintering and traction induced deformation. Acta Metall. 1988;36(9):2551–61.
40. Fischmeister HF, Arzt E. Densification of powders by particle deformation. Powder Metall. 1983;26(2):82–8.
41. Arzt E. The influence of an increasing particle coordination on the densification of spherical powders. Acta Metall. 1982;30(10):1883–90.
42. Okuma G, Kadowaki D, Hondo T, Tanaka S, Wakai F. Interface topology for distinguishing stages of sintering. Sci Rep. 2017;7(1):1–9.
43. Potyondy DO, Cundall PA. A bonded-particle model for rock. Int J Rock Mech Min Sci. 2004;41(8):1329–64.
44. Rycroft C. Voro++: a three-dimensional Voronoi cell library in C++. Berkeley, CA: Lawrence Berkeley National Lab. (LBNL); 2009. 2009/01/15/. Report No.: LBNL-1432E.
45. Mackenzie JK, Shuttleworth R. A phenomenological theory of sintering. Proc Phys Soc B. 1949;62(12):833.
46. German RM. Coordination number changes during powder densification. Powder Technol. 2014;253:368–76.
47. Jagota A, Dawson PR. Micromechanical modeling of powder compacts—II. Truss formulation of discrete packings. Acta Metall. 1988;36(9):2563–73.
48. Rahaman MN, De Jonghe LC. Sintering of spherical glass powder under a uniaxial stress. J Am Ceram Soc. 1990;73(3):707–12.
49. Scherer GW, Bachman DL. Sintering of low-density glasses: II. J Am Ceram Soc. 1977;60(5–6):239–43.
50. Bordia RK, Scherer GW. On constrained sintering—I. Constitutive model for a sintering body. Acta Metall. 1988;36(9):2393–7.
51. Scherer GW. Viscous sintering under a uniaxial load. J Am Ceram Soc. 1986;69(9):C-206.
52. Scherer GW. Sintering with rigid inclusions. J Am Ceram Soc. 1987;70(10):719–25.
53. Pilkey WD, Pilkey DF, Peterson RE. Peterson's stress concentration factors, 3rd edn. Hoboken, NY: John Wiley & Sons, 2008; p. 560.
54. Thouless MD. Bridging and damage zones in crack growth. J Am Ceram Soc. 1988;71(6):408–13.
55. Sudre O, Lange FF. The effect of inclusions on densification: III, The desintering phenomenon. J Am Ceram Soc. 1992;75(12):3241–51.
56. Thouless MD, Evans AG. Some considerations regarding the creep crack growth threshold. Scr Metall. 1984;18(10):1175–80.

57. Anderson TL. Fracture mechanics: fundamentals and applications, 3rd edn. Boca Raton, FL: CRC Press; 2005.
58. Thouless MD, Hsueh CH, Evans AG. A damage model of creep crack growth in polycrystals. Acta Metall. 1983;31(10):1675–87.
59. Goodier JN. Slow viscous flow and elastic deformation. Lond Edinb Dubl Phil Mag. 1936;22(148):678–81.
60. Scherer GW. Sintering inhomogeneous glasses: application to optical waveguides. J Non-Cryst Solids. 1979;34(2):239–56.
61. Glinka G, Newport A. Universal features of elastic notch-tip stress fields. Int J Fatigue. 1987;9(3):143–50.
62. Hayhurst DR, Morrison CJ, Leckie FA. The effect of stress concentrations on the creep rupture of tension panels. J Appl Mech. 1975;42(3):613–8.
63. Hertzberg RW. Deformation and fracture mechanics of engineering materials. Wiley. 1989;1989/01/17/:714 p.
64. Boccaccini AR, Ondracek G, Mombello E. Determination of stress concentration factors in porous materials. J Mater Sci Lett. 1996;15(6):534–6.
65. Thouless MD. A review of creep rupture in materials containing an amorphous phase. Res Mech. 1987;22(3):213–42.
66. Evans AG, Blumenthal WR. High temperature failure in ceramics. In: Bradt RC, Evans AG, Hasselman DP, Lange FF, editors. Fracture mechanics of ceramics: Surface flaws, statistics, and microcracking. International Symposium on the Fracture Mechanics of Ceramics, vol. 5. New York, NY: Plenum Press, 1983; p. 423–48.
67. Dimelfi RJ, Nix WD. The stress dependence of the crack growth rate during creep. Int J Fract. 1977;13(3):341–8.
68. Evans AG, Dalgleish BJ. Some aspects of the high temperature performance of ceramics and ceramic composites. Ceram Eng Sci Proc. 1986;7:1073–94.
69. Van Leeuwen HP. The application of fracture mechanics to creep crack growth. Eng Fract Mech. 1977;9(4):951–74.
70. Thouless MD, Evans AG. On creep rupture in materials containing an amorphous phase. Acta Metall. 1986;34(1):23–31.
71. Nicholson RD, Formby CL. The validity of various fracture mechanics methods at creep temperatures. Int J Fract. 1975;11(4):595–604.
72. Riedel H, Zipse H, Svoboda J. Equilibrium pore surfaces, sintering stresses and constitutive equations for the intermediate and late stages of sintering—II. Diffusional densification and creep. Acta Metall Mater. 1994;42(2):445–52.

How to cite this article: Carazzone JR, Martin CL, Cordero ZC. Crack initiation, propagation, and arrest in sintering powder aggregates. *J Am Ceram Soc*. 2020;00:1–20. https://doi.org/10.1111/jace.17170